MNRAS **000**, 000–000 (0000) Preprint 19th October 2018 Compiled using MNRAS LATEX style file v3.0

Energy budget and envelope unbinding in common envelope evolution

Luke Chamandy,[1]★ Yisheng Tu,[1] Eric G. Blackman, [1]†, Jonathan Carroll-Nellenback,[1] Baowei Liu,[1] Jason Nordhaus[2,3] and Adam Frank[1]‡
[1]*Department of Physics and Astronomy, University of Rochester, Rochester NY 14618, USA*
[2]*National Technical Institute for the Deaf, Rochester Institute of Technology, NY 14623, USA*
[3]*Center for Computational Relativity and Gravitation, Rochester Institute of Technology, NY 14623, USA*

19th October 2018

ABSTRACT
We analyze a 3D hydrodynamic simulation of common envelope evolution to understand how energy is transferred between various forms leading to the partial unbinding of the envelope. It is found that 14% of the envelope is unbound during the simulation, though this value could be higher or lower depending on the definition of 'unbound' that is adopted. Essentially all of the unbinding occurs between the beginning of the simulation and the end of the rapid plunge-in phase, here defined to coincide with the first periastron passage. By contrast, the total envelope energy is roughly constant during this time because positive energy transferred to the gas is counterbalanced by an increase in negative binding energy due to the closer proximity of the inner layers to the plunged-in secondary. Subsequently, during the slow spiral-in phase, energy continues to be transferred from the red giant core-secondary particle system to the envelope at a rather steady rate, and we discuss the possibility of complete ejection or merger at times much longer than the duration of the simulation. We critically assess the so-called α-energy prescription in the light of these findings, and suggest an alternative formulation. In addition, we propose that the relative motion between the centre of mass of the envelope and that of the red giant core-secondary system could account for the offsets of planetary nebula central stars from the geometric centres of their nebulae in at least some cases, and that this relative motion should also be taken into account when assessing the extent to which the envelope is bound.

1 INTRODUCTION

• Observations, direct and indirect, of very close binaries believed to be the result of CEE.

• Examples include central stars of PNe an pPNe, progenitors of BH-BH and NS-NS mergers, high- and low-mass X-ray binaries, and probably SNe type Ia (Ivanova et al. 2013).

• Implication is that a merger is prevented in a large fraction [Luke comments: (need a quantitative estimate)] of cases (REF).

• For this to happen must stabilize orbit by removing drag force.

• Simplest way to achieve this is by complete removal of the envelope, but in reality removal may not need to be complete (REF).

• Energy formalism was developed to predict the fate of a given binary system.

• In this prescription the two possible fates are merger or envelope ejection, but which it is depends on $\alpha_{\rm CE}$ which is a poorly constrained parameter.

• Thus far the envelope has not been ejected in 3D hydro simulations unless an additional energy source (recombination energy) is introduced.

• The role of recombination energy is very controversial and it is not at all clear whether it is important enough to explain envelope ejection.

• Envelope ejection in simulations seems to be harder than expected (based on observations and theory; REFS).

• The reason may come down to

1) Limitations of the theory (unjustified approximations, missing physics).
2) Limitations of the simulations (unrealistic initial conditions, small duration, limited resolution, missing physics).

• Missing physics may include extra sources of energy, like recombination energy, accretion energy, nuclear energy, etc.

• The goal of this work is to account for the various energy terms in the simulation as accurately as possible, and in so doing shed light on the envelope ejection process. Pertinent questions are as follows:

1) How does the energy transition from one form to another with time, and in what proportion does the liberated orbital energy get transferred to the various other forms of energy?
2) What are the expectations for envelope removal and energy transfer from analytic theory based on the CE energy formalism, and to what extent do these expectations concur with simulation results?
3) The theory contains an explicit uncertainty absorbed into the factor $\alpha_{\rm CE}$. What is the value of $\alpha_{\rm CE}$ from the simulations and what is the explanation for this value in the simulation?
4) To the extent that analytical expectations and simulation results do not agree, what are the reasons for this, and does this suggest any modifications in either the analytics or the simulations, e.g. the inclusion of missing terms in the theory or the inclusion of extra physics in the simulations?
5) Regardless of the level of agreement between theory and sim-

ulations, one could imagine making the simulations more realistic by including certain physical processes, like mixing due to convection or new energy sources; what effects would including this new physics have on envelope ejection?
6) The simulations are limited in that they can afford computationally to explore only a portion of the CE phase. In reality, this phase starts earlier (from the Roche lobe overflow mass transfer phase) and likely ends much later; what are the implications of this extra time (and altered initial conditions) for envelope removal?

1.1 Summary of relevant references

- Sandquist et al. (1998)

  – Plots energy terms vs time (Fig 1).
  – Compares for initial condition with or without rotation of primary (Fig 1) and finds little difference.
  – Plots various mass components including bound mass vs time in Fig 8 (see also Figs 14 and 15 for other sims).

- Sandquist et al. (2000)
- Ricker & Taam (2008) (apparently does not contain much of relevance)
- Passy et al. (2012)

  – Virtually all of the mass that becomes unbound does so within the first 50 days (Sec. 4.1) and this seems to correspond to a time between the first periastron passage and first apastron passage (Fig 4).
  – In their SPH simulations they determine the initial radius in the envelope of those particles which have become unbound by the end of the simulation (Fig 10).
  – From this figure there is about an equal contribution from all radii at radii greater than half the stellar radius, and a much smaller contribution for radii less than half the stellar radius (Fig 10).

- Ricker & Taam (2012)

  – They simulate a $1.05\,\mathrm{M}_\odot$ red giant with a $0.36\,\mathrm{M}_\odot$ core and a $0.6\,\mathrm{M}_\odot$ companion.
  – They find that by the end of the simulation 26% of the mass has been unbound, and that the mass loss rate is fairly steady (Fig 9) (of this 25% about 4% ($0.3\,\mathrm{M}_\odot$ out of $0.18\,\mathrm{M}_\odot$) is already unbound at $t = 0$).
  – The mass loss rate at the end of the simulation is $\sim 2\,\mathrm{M}_\odot\,\mathrm{yr}^{-1}$.
  – They obtain a local peak in the unbound mass with time at approximately the location of the first periastron passage (as we do; see their Figs. 9 and 2).
  – Defines the 'energetic efficiency of mass outflow' as 'the ratio of the energy required to unbind the ejected part of the envelope to the energy released by the inspiralling cores.' (This is in principle hard to calculate and they estimate it from their initial and final conditions).
  – About 75% of the energy released by the inspiralling cores is estimated to go into the part of the envelope that remains bound, while the rest goes into unbinding material.
  – If the mass loss rate at the end of the simulation continues to be constant, then the envelope would become unbound within two additional months.

- Nandez et al. (2014)

  – KE and unbound mass rise at same time and then unbound mass flattens (Fig 8; top panel includes internal energy in definition of unbound). This also coincides with the end of plunge-in (although the separation vs time graph is not shown for that sim 376, had to reference table 3).
  – Mass unbinding is bursty as shown in Fig 11.
  – Follows KE of unbound particles with time (Fig 12)

- Nandez et al. (2015)

  – Find that 'between 1/4 and 1/2 of the released orbital energy is taken away by the ejected material.' (abstract)

- Nandez & Ivanova (2016) (apparently does not contain much of relevance)
- Ivanova & Nandez (2016)

  – "...we cannot detect the orbital energy deposition inside the binary orbit, but outside of the orbit it affects the entire envelope, primarily changing the mechanical energy of the envelope– the potential energy and the kinetic energy (and kinetic energy is converted to the potential energy with time)..."
  – Identify 4 different phases of mass ejection (Sec 8).
  – They include recombination energy.

- Staff et al. (2016a) (apparently does not contain much of relevance)
- Staff et al. (2016b) (apparently does not contain much of relevance)
- Kuruwita et al. (2016) (not directly relevant especially because lots of outflow of mass outside of simulation box)
- Kruckow et al. (2016) Discusses energy formalism for massive binaries (need to read it more carefully)
- Ohlmann et al. (2016)

  – Analyzed total energy budget of envelope but in a way that did not completely isolate the separate physical contributions.
  – Found that 8% of envelope mass is ejected by end of their simulation (with similar parameters to ours) at $t \sim 120$ d.
  – Found that most of this material is expelled in the first 40 days.
  – Found that after $t = 40$ d the mass loss rate settles to about $0.015\,\mathrm{M}_\odot\,\mathrm{yr}^{-1}$.
  – Argue that similar systems are observed to have ejected the envelope.
  – Hence conclude that either need longer timescales or additional energy sources.

- Iaconi et al. (2017)

  – Analyzed energy budget but much of the gas left the box early on which makes analysis difficult (Fig 14) for the enzo simulation.
  – But this not a problem from phantom simulation (Fig 14 bottom panel).
  – Literature review of unbound mass fraction in CE simulations (Tab. 1 and Sec 4.5).

- Clayton et al. (2017) claim that episodic mass ejections over tens of years can unbind the envelope (they use 1D simulations).
- Iaconi et al. (2018)

  – Find that fraction of envelope that is unbound increases with resolution (Fig. 4)
  – Discussion of the energy needed to unbind the remaining *bound* mass (Sec 7.2)
  – Discussion of the unbinding efficiency with reference to the alpha prescription (Sec 7.3)

– Calculates that there is enough energy release to unbind the envelope but that this does not happen because the distribution of energy is inefficient. We need to redo such an analysis but more carefully.

– They find a trend (in agreement with Passy+12) that less massive secondaries unbind less of the envelope even though they inspiral deeper.

2 SIMULATION OVERVIEW

The simulation analyzed is Model A of Paper I, which involves the interaction between a $2.0\,M_\odot$ red giant (RG) primary with a $0.4\,M_\odot$ point particle core and a $1.0\,M_\odot$ point particle representing a white dwarf (WD) or main sequence secondary. Unlike Model B of that paper, Model A did not have a subgrid model for accretion onto the secondary, and Model A is chosen for the present study partly because of its simplicity in this respect. We refer the reader to Paper I for a more detailed description of the simulation setup, but here we summarize the salient features.

The hydrodynamic simulation was performed using the 3D adaptive mesh refinement code AstroBEAR (Cunningham et al. 2009; Carroll-Nellenback et al. 2013), and accounts for all gravitational interactions (particle-particle, particle-gas, and gas-gas). The RG density and pressure profiles were initialized using a procedure similar to that outlined by Ohlmann et al. (2017) (for details see Paper I). The simulation was initialized with the stars undergoing a circular orbit at $t = 0$ with orbital separation $a|_{t=0} = 49.0\,R_\odot$, slightly larger than the RG radius of $R_1 = 48.1\,R_\odot$, and was terminated at $t = 40$ d. The mesh was refined at the highest level with voxel dimension $\delta = 0.14\,R_\odot$ before $t = 16.7$ d and $\delta = 0.07\,R_\odot$ thereafter *everywhere* inside a large spherical region centered on the point particles. The initial radius of this maximally resolved region was $r_{\rm refine} = 72\,R_\odot$ and at all times $r_{\rm refine} > 2.5a$. The spline softening radius for both particles was set to $r_{\rm soft} \approx 17\delta$ for the entire simulation.

3 ENERGY BUDGET

In the top panel of Figure 1 we present the time-evolution of each energy component, integrated over the simulation domain. Times of apastron and periastron passages are labeled on the axis by long blue or short orange tick marks, respectively. Expressions for the various contributions, as well as their values at $t = 0$, $t = 13$ d and $t = 40$ d, are given in Tab. 1. The time $t = 13$ d is chosen because it is the approximate time of first periastron passage and is thus a reasonable choice for marking the end of the plunge-in phase and the beginning of the slow spiral-in phase. The inter-particle separation goes from $a = 49.0\,R_\odot$ at $t = 0$ to $a = 14.1\,R_\odot$ at $t = 13$ d and $a = 7.8\,R_\odot$ at $t = 40$ d.

A key result is that the potential energy term involving gas and the secondary is important even when the secondary is situtated just outside the RG surface (at $t = 0$) and at the end of plunge-in at $t = 13$ d this term contributes almost half of the potential energy associated with the gas. Moreover, the net energy tranferred to the gas from $t = 0$ until $t = 13$ d is $< 0.1 \times 10^{47}$ erg, so rather negligible. At first glance this is surprising given that essentially all of the unbinding of envelope material occurs during this time (Section 4). However, it has a simple explanation. The plunge-in of the secondary serves to violently disrupt and energize the outer layers of the envelope, while at the same time leading to the secondary occupying a deeper position within the envelope, which results in a stronger pull of the inner layers toward the centre. Thus the gain in gas kinetic energy is offset by an increase in negative potential energy, leading to almost zero net gain, and therefore negligible exchange between net particle and net gas energy during this time.

From the particle point of view, we would naively expect the particle energy to decrease significantly during plunge-in (transferring energy to the gas), though it does not. Although the particles are getting closer together between $t = 0$ d and $t = 13$ d, we are not dealing here with a simple two-body problem because of the force exerted on the particles by the gas. This interaction causes the net particle kinetic energy to increase by almost as much as the negative potential energy between $t = 0$ d and $t = 13$ d, resulting in zero net change. Subsequently, after $t \approx 15$ d, the particles tranfer energy to the gas at a roughly constant rate as they spiral in closer together. In the subsections below we expand on these points and discuss each of the curves in the top panel of Figure 1 in detail.

3.1 Total energy

The total energy is plotted in solid black and changes by 5% between the start of the simulation and $t = 40$ d (a dotted horizontal grey line shows the initial value for reference). The total energy rises gradually, except for a dip after $t = 16.7$ d corresponding to the time that the softening radius around both particles, as well as the size of the smallest resolution element δ, were halved. This discontinuity is expected because reducing the spline softening radius from $r_{\rm soft} = r_{\rm soft,0}$ to $r_{\rm soft} = r_{\rm soft,0}/2$ immediately strengthens the gravitational force for $r < r_{\rm soft,0}$, and thus leads to greater (in magnitude) particle-gas potential energy components [Luke comments: we must compare the size of the jump with the expected value as a check.]. 16% of the net increase in energy during the simulation is caused by inflow of the ambient medium from the domain boundaries. The remaining error may be caused by the finite time step in the simulation, which leads to particle orbits that are not completely smooth, or by small errors introduced by the multipole Poisson solver. This small variation in the total energy does not affect the conclusions of the present study.

3.2 Particle and gas contributions

The solid green and solid orange lines in the top panel of Figure 1 show the particle orbital energy E_{1-2} and total gas energy $E_{\rm gas}$, respectively. The quantity E_{1-2} is equal to the sum of the quantities shown by the blue curves relating to particle-only energy terms (namely the kinetic energies of both particles and their mutual potential energy), while $E_{\rm gas}$ is equal to the sum of the quantities shown by the red and purple curves, relating to gas-only and gas-particle energy terms, respectively. Their sum $E_{1-2} + E_{\rm gas}$ gives the total energy of the system $E_{\rm tot}$ (solid black). By referring to the green and orange curves we see how the orbital energy of the particles is gradually transferred to the gas, and that this transfer starts around the time that the plunge-in phase ends. To understand the energy evolution in greater detail, it is necessary to study the relationships between individual energy terms, and we do this below.

3.3 Particles

Energy terms pertaining to the particles only (RG core primary, labeled with subscript '1' and hereafter referred to as 'particle 1,' and secondary, labeled with subscript '2' and hereafter referred to as 'particle 2') are shown in blue. The kinetic energy of particle 1

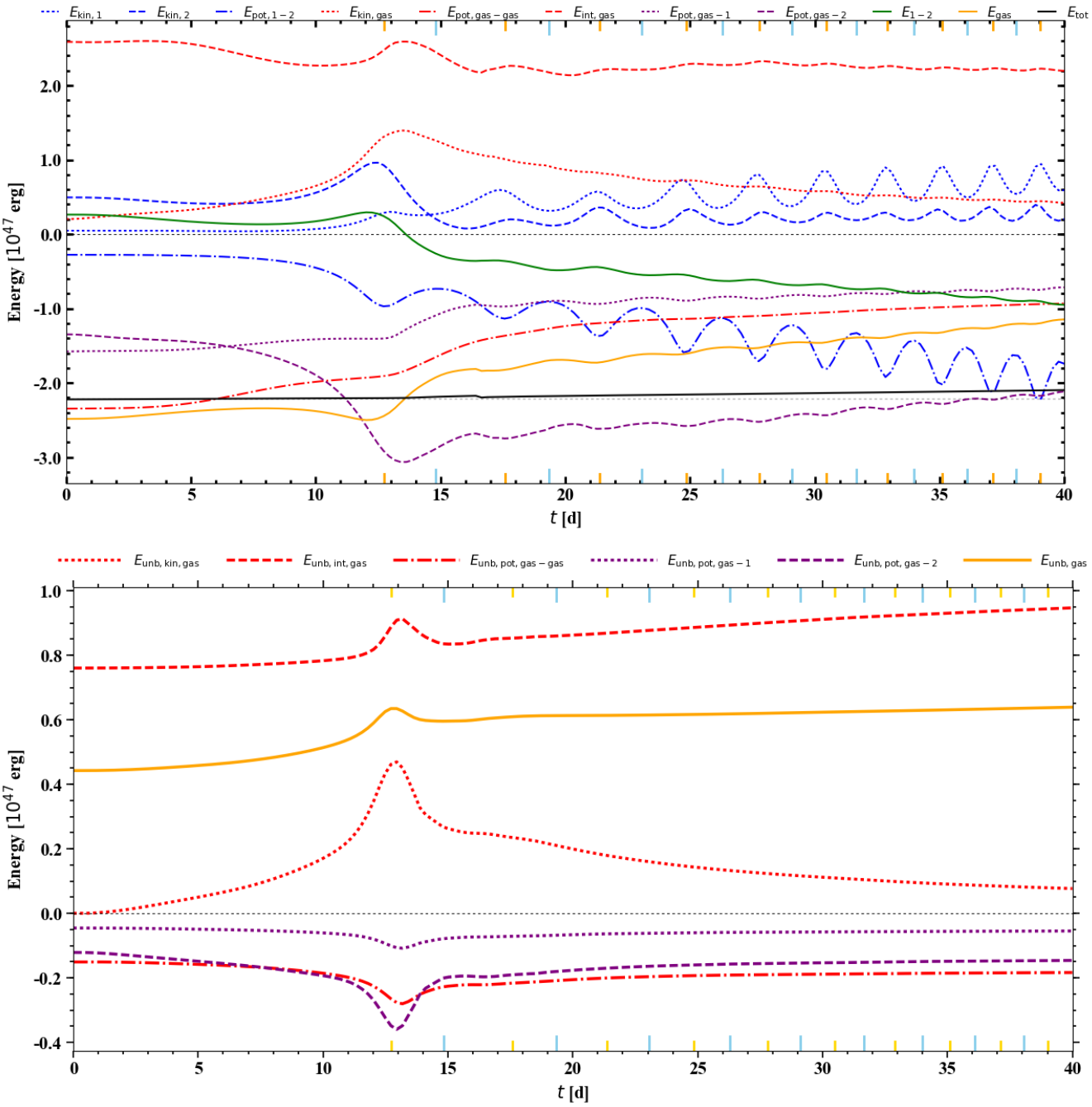

Figure 1. Top: Evolution of the various energy components integrated over the simulation domain. Those involving only particles are plotted in blue, only gas in red, and those involving gas and particles are plotted in purple. Total energy is shown by a black line, with its initial value plotted as a grey dashed line for reference. Green and orange solid lines show the total particle and gas energies, respectively, with terms involving both particles and gas counting toward the total gas energy. A discontinuity at $t = 16.7$ d is caused by the change in the spline softening length of both particles from $2.4\,\mathrm{R}_\odot$ to $1.2\,\mathrm{R}_\odot$. The sampling rate of the data plotted is about one frame every 0.23 d. Times of apastron and periastron passage are shown as long blue and short orange tick marks, respectively. Bottom: As in the top panel but now showing the energy of the unbound gas only, where 'unbound' is defined as $\mathcal{E}_{\rm gas} \geqslant 0$. Note the difference in vertical axis range compared to the top panel.

$E_{\rm kin,1}$ (dotted blue) first remains steady and then gradually rises as the inter-particle separation reduces. It oscillates in approximate synchrony with the orbit, with maxima in kinetic energy coinciding with periastron passages, as would be expected. The kinetic energy of particle 2 $E_{\rm kin,2}$ (dashed blue) first increases during plunge-in, which we here define as occurring between $t = 8$ and $t = 13$ d. It then decreases rather sharply, which is explained by the fact that the secondary initially orbits the RG (core+envelope) but eventually orbits (roughly speaking) only particle 1 along with a small fraction of the original envelope gas occupying the region $|\boldsymbol{x} - \boldsymbol{x}_1| < a$. Following this decrease, $E_{\rm kin,2}$ then rises less rapidly than $E_{\rm kin,1}$, as there is competition between reduced particle separation and

Table 1. Terms in the energy budget, in units of 10^{47} erg, integrated over the simulation domain. Values are shown for the start of the simulation $t = 0$, end of plunge-in $t = 13\,\mathrm{d}$, and end of the simulation $t = 40\,\mathrm{d}$. Also shown are the changes in the values between these times.

Energy component	Symbol	Expression	$t = 0$	$t = 13\,\mathrm{d}$	$t = 40\,\mathrm{d}$	$\Delta E_{0-13\,\mathrm{d}}$	$\Delta E_{13-40\,\mathrm{d}}$	$\Delta E_{0-40\,\mathrm{d}}$
Particle 1 kinetic	$E_{\mathrm{kin},1}$	$\frac{1}{2}M_{1,\mathrm{c}}v_{1,\mathrm{c}}^2$	0.05	0.30	0.59	0.25	0.29	0.54
Particle 2 kinetic	$E_{\mathrm{kin},2}$	$\frac{1}{2}M_2v_2^2$	0.49	0.86	0.20	0.37	−0.66	−0.29
Particle-particle potential	$E_{\mathrm{pot},1-2}$	$-\mathrm{G}M_{1,\mathrm{c}}M_2/a$	−0.28	−0.96	−1.74	−0.69	−0.78	−1.46
Gas bulk kinetic	$E_{\mathrm{kin,gas}}$	$\frac{1}{2}\int\rho(\boldsymbol{x})v_{\mathrm{gas}}^2(\boldsymbol{x})\mathrm{d}\boldsymbol{x}$	0.20	1.35	0.42	1.15	−0.93	0.22
Gas internal	$E_{\mathrm{int,gas}}$	$\frac{3}{2}\int P(\boldsymbol{x})\mathrm{d}\boldsymbol{x}$	2.59	2.53	2.19	−0.06	−0.33	−0.39
Gas-gas potential	$E_{\mathrm{pot,gas-gas}}$	$\frac{1}{2}\int\Phi_{\mathrm{gas}}(\boldsymbol{x})\rho(\boldsymbol{x})\mathrm{d}\boldsymbol{x}$	−2.35	−1.90	−0.93	0.45	0.97	1.41
Gas-particle 1 potential	$E_{\mathrm{pot,gas-1}}$	$-\mathrm{G}M_{1,\mathrm{c}}\int(\rho(\boldsymbol{x})/\lvert\boldsymbol{x}-\boldsymbol{x}_{1,\mathrm{c}}\rvert)\mathrm{d}\boldsymbol{x}$	−1.58	−1.40	−0.72	0.18	0.68	0.86
Gas-particle 2 potential	$E_{\mathrm{pot,gas-2}}$	$-\mathrm{G}M_2\int(\rho(\boldsymbol{x})/\lvert\boldsymbol{x}-\boldsymbol{x}_2\rvert)\mathrm{d}\boldsymbol{x}$	−1.35	−2.99	−2.12	−1.64	0.87	−0.77
Particle total	E_{1-2}	$E_{\mathrm{kin},1}+E_{\mathrm{kin},2}+E_{\mathrm{pot},1-2}$	0.26	0.20	−0.95	−0.06	−1.15	−1.21
Gas total	E_{gas}	$E_{\mathrm{kin,gas}}+E_{\mathrm{int,gas}}+\sum_j E_{\mathrm{gas-j}}$	−2.49	−2.40	−1.15	0.08	1.25	1.33
Total	E_{tot}	$E_{1-2}+E_{\mathrm{gas}}$	−2.22	−2.20	−2.10	0.02	0.10	0.12

Table 2.

Energy component at $t = 0$	Symbol	Expression	Red giant $a_\mathrm{i} = 49\,\mathrm{R}_\odot$	Red giant $a_\mathrm{i} = 109\,\mathrm{R}_\odot$	Asymptotic giant $a_\mathrm{i} = 124\,\mathrm{R}_\odot$	Asymptotic giant $a_\mathrm{i} = 284\,\mathrm{R}_\odot$
Particle 1 kinetic	$E_{\mathrm{kin},1,\mathrm{i}}$	$\frac{1}{2}M_{1,\mathrm{c}}v_{1,\mathrm{c}}^2$	0.05	0.02	0.03	0.01
Particle 2 kinetic	$E_{\mathrm{kin},2,\mathrm{i}}$	$\frac{1}{2}M_2v_2^2$	0.49	0.22	0.17	0.07
Particle-particle potential	$E_{\mathrm{pot},1-2,\mathrm{i}}$	$-\mathrm{G}M_{1,\mathrm{c}}M_2/a$	−0.28	−0.12	−0.16	−0.07
Envelope bulk kinetic	$E_{\mathrm{kin,e,i}}$	$\frac{1}{2}m_\mathrm{e}v_{1,\mathrm{i}}^2$	0.20	0.09	0.07	0.03
Envelope internal	$E_{\mathrm{int,e,i}}$	$4\pi\int_0^{R_1}\frac{P}{\gamma-1}r^2dr$	1.81	1.81	0.71	0.71
Envelope-envelope potential	$E_{\mathrm{pot,e-e,i}}$	$-(4\pi)^2\mathrm{G}\int_0^{R_1}\rho(r)r\int_0^r\rho(r')r'^2dr'dr$	−2.13	−2.13	−0.57	−0.57
Envelope-particle 1 potential	$E_{\mathrm{pot,e-1,i}}$	$-4\pi\mathrm{G}m_{1,\mathrm{c}}\int_0^{R_1}\rho r dr$	−1.56	−1.56	−0.88	−0.88
Envelope-particle 2 potential	$E_{\mathrm{pot,e-2,i}}$	$\frac{\mathrm{G}m_2m_\mathrm{e}}{a_\mathrm{i}}$	−1.20	−0.54	−0.37	−0.16
Particle total	$E_{1-2,\mathrm{i}}$	$E_{\mathrm{kin},1,\mathrm{i}}+E_{\mathrm{kin},2,\mathrm{i}}+E_{\mathrm{pot},1-2,\mathrm{i}}$	0.26	0.12	0.04	0.02
Envelope total	$E_{\mathrm{e,i}}$	$E_{\mathrm{kin,e,i}}+E_{\mathrm{int,e,i}}+\sum_j E_{\mathrm{e-j,i}}$	−2.87	−2.32	−1.05	−0.88
Total particle and envelope	$E_{1-2-\mathrm{e,i}}$	$E_{1-2,\mathrm{i}}+E_{\mathrm{e,i}}$	−2.61	−2.21	−1.01	−0.86

Table 3.

	a_i [$\mathrm{R}_\odot$]	LHS [10^{47} erg]	RHS($a_\mathrm{f} = 7\,\mathrm{R}_\odot$) [$10^{47}$ erg]
Eq. (3)	49	1.9	$0.2\alpha_{\mathrm{CE}}$
Eq. (3)	109	1.9	$0.6\alpha_{\mathrm{CE}}$
Eq. (4)	49	2.9	$1.2\alpha_{\mathrm{CE}}$
Eq. (4)	109	2.3	$1.1\alpha_{\mathrm{CE}}$

Table 4.

		a_i ($\mathrm{R}_\odot$)	a_f ($\mathrm{R}_\odot$) $\alpha_{\mathrm{CE}} = 0.1$	0.25	0.5	1
RGB	Eq. (3)	49	0.3	0.8	1.5	2.6
$\lambda = 1.31$		109	0.4	0.9	1.7	3.1
	Eq. (4)	49	0.2	0.6	1.2	2.6
		109	0.3	0.7	1.5	3.1
AGB	Eq. (3)	124	1.3	3.0	5.6	9.8
$\lambda = 0.91$		284	1.3	3.2	6.2	11.5
	Eq. (4)	124	0.9	2.4	4.8	9.8
		284	1.1	2.8	5.7	11.5

loss of gas mass interior to the orbit. Naturally, $E_{\mathrm{kin},2}$ undergoes oscillations in phase with those of $E_{\mathrm{kin},1}$.

The potential energy of the system of particles $E_{\mathrm{pot},1-2}$ (that is excluding that due to the gas-particle gravitational forces) is shown in dash-dotted blue, and its mean value over an orbit reduces by about 1.7×10^{47} erg between $t = 0$ and $t = 40\,\mathrm{d}$. Its overall steady decrease even at $t = 40\,\mathrm{d}$ is evidence that the evolution of the system continues unabated even as the rate of change of the mean inter-particle separation $\dot{\bar{a}}(< 0)$ (where overbar denotes mean) reduces in magnitude (Paper I) so that $\ddot{\bar{a}} > 0$. Qualitatively, this behaviour is as expected from the $1/a$ Newtonian potential which for a circular orbit would give $\dot{E}_{\mathrm{pot},1-2} \propto \dot{a}/a^2$; the decrease in $|\dot{a}|$ competes with the reduction in a and whether $\ddot{E}_{\mathrm{pot},1-2}$ is positive or negative is not immediately obvious and will depend on the details of the orbital evolution.

3.4 Gas

Energy terms which relate to the gas only are shown in red. The total bulk kinetic energy of gas $E_{\mathrm{kin,gas}}$ (dotted red) rises during plunge-in as envelope material is violently propelled outward, and sub-

sequently gradually reduces as the expanding envelope is decelerated by gravity and shocks. The dashed red curve shows the internal energy of the gas $E_{\rm int,gas}$, of which about $0.8{\times}10^{47}$ erg is contributed by the ambient medium, which has a pressure of 1×10^5 dyn cm^{-2} and fills the simulation domain with side $1150\,{\rm R}_\odot$. On the other hand, the ambient medium hardly contributes to $E_{\rm kin,gas}$ since the bulk motions within it are small. Initially, $E_{\rm int,gas}$ is fairly steady, but then undergoes relatively small variations due to expansion and compression of gas. Both $E_{\rm int,gas}$ and $E_{\rm kin,gas}$ show small-amplitude oscillations with maxima approximately coinciding with periastron passages.

Each close encounter of the particles leads to a 'dredging up' of material in dual spiral wakes. During plunge-in, most of the resulting energy imparted to the gas is in the form of bulk kinetic energy, but the gas also receives a significant amount of internal energy, which is expected from the spiral shock morphology observed. The subsequent slow decrease of $E_{\rm kin,gas}$ is accompanied by a corresponding increase in the potential energy due to gas self-gravity $E_{\rm pot,gas-gas}$ (dash-dotted red). Of the total $E_{\rm pot,gas-gas}$, relatively small amounts 0.2×10^{47} erg and 0.1×10^{47} erg are contributed, respectively, by the gravitational interaction between the ambient medium and envelope and by that of the ambient medium with itself. Between $t = 0$ and $t = 40\,{\rm d}$, a substantial amount of work 1.4×10^{47} erg is done in expanding the envelope against its own gravity. In principle, unbinding the gas from the particles does not necessarily require the gas to become unbound from *itself*. Our results show, however, that in practice much of the energy can go into expanding the envelope against self-gravity.

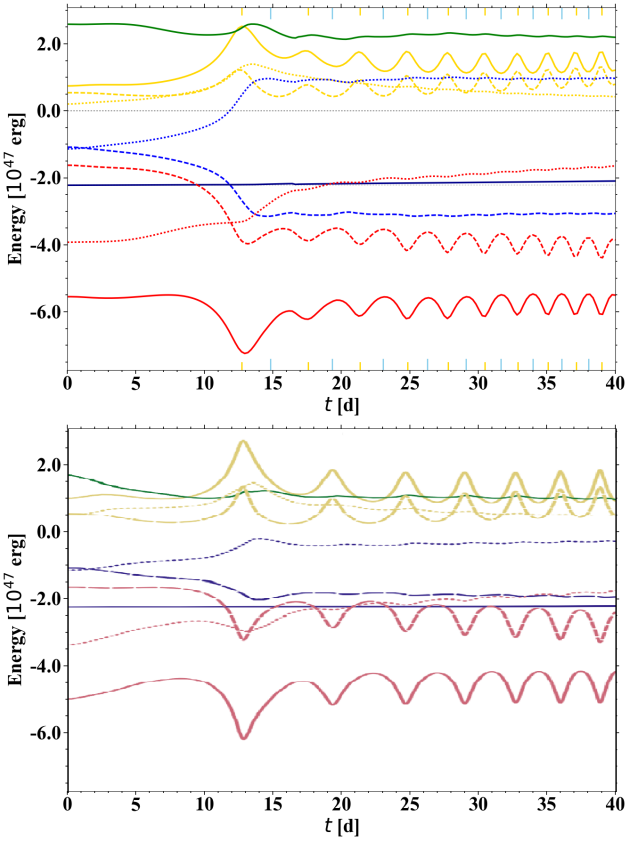

Figure 2. Comparison between energy terms (integrated over the simulation domain) in our simulation (top) and in the simulation of Ohlmann et al. (2016) (bottom, adapted from the latter work). Legend labels are the same as those of Ohlmann et al. (2016): 'total' (solid blue), 'kinetic' (solid yellow), 'potential' (solid red), 'internal' (solid green), 'total envelope' (dotted blue), 'kinetic envelope' (dotted yellow), 'potential envelope' (dotted red), 'total cores' (dashed blue), 'kinetic cores' (dashed yellow) and 'potential cores' (dashed red). In the upper panel the contribution from $E_{\rm pot,gas-2}$ is included in the 'particle potential energy,' 'gas potential energy' and 'total particle energy' terms, but these terms do not include the contribution from $E_{\rm pot,gas-1}$. On the other hand, the contribution from $E_{\rm pot,gas-1}$ is included in the total gas energy but the contribution from $E_{\rm pot,gas-2}$ is not so included. These choices were made to obtain a high level of agreement with the results of Ohlmann et al. (2016), where the precise allocation of each contribution was not apparent to us.

3.5 Gas-particles interaction

The purple curves show the potential energy terms accounting for the gas-particle 1 gravitational force $E_{\rm pot,gas-1}$ (dotted purple) and gas-particle 2 gravitational force $E_{\rm pot,gas-2}$ (dashed purple). These terms must be included in the energy budget of the envelope when assessing the extent to which it is bound. The contribution to these terms from the ambient medium is rather negligible ($< 0.2{\times}10^{47}$ erg total). Initially the inner layers of the RG are generally unaffected by the interaction with the secondary, which explains the slow variation in $E_{\rm pot,gas-1}$ up until the plunge-in, when the inner part of the envelope is strongly disrupted. After the end of plunge-in at $t = 13\,{\rm d}$, $E_{\rm pot,gas-1}$ shows an increase with time as envelope material is transported outward. Thus, work must be done to expand the envelope against the gravitational force toward particle 1, situated roughly at its centre.

What is less straightforward, and sometimes neglected in simple analyses based on the CE energy formalism, is the gravitational interaction between gas and particle 2 (dashed purple). Even at $t = 0$, $E_{\rm pot,gas-2}$ is important, having almost equal magnitude to $E_{\rm pot,gas-1}$ (particle 1 is closer to the bulk of the gas but particle 2 is more massive). However, as particle 2 plunges in toward the envelope centre, $E_{\rm pot,gas-2}$ increases in magnitude by $1.6{\times}10^{47}$ erg and at the end of plunge-in at $t = 13\,{\rm d}$ it is the most important contribution to the gas potential energy. From the beginning of the simulation until the end of plunge-in, $E_{\rm gas}$ gains only about 0.1×10^{47} erg, or about 3%. Thus, the liberation of orbital energy as particle 2 plunges in does not come "for free" because with the mass M_2 now close to the envelope centre, the envelope is bound inside a much deeper potential well. After plunge-in, from $t = 13\,{\rm d}$ to $t = 40\,{\rm d}$, we see that the envelope expands to become less bound at the expense of the gas kinetic energy (dotted red) and particle-particle potential energy (dash-dotted blue), and that significant work is expended in moving gas outward against the gravitational force due to particle 2, as well as that due to particle 1 and gas self-gravity.

3.6 Comparison with previous work

We used almost the same parameter values and initial conditions as Ohlmann et al. (2016) and thus it is useful to compare directly their results and ours. In the top panel of Figure 2 we plot the energy terms as in Figure 2 of Ohlmann et al. (2016), and in the bottom panel we show a version of their figure with the time axis truncated at $t = 40\,{\rm d}$. The curves are as described in the legend but Ohlmann et al. (2016) used a different kind of code and it was not clear to us precisely how the different energy components were divided among the various curves. We found that close agreement was obtained if the curves labeled as "particle potential energy," "gas potential energy" and "total particle energy" (dashed red, dotted red and

dashed blue, respectively) include the contribution from $E_{\rm pot,gas-2}$ but not from $E_{\rm pot,gas-1}$, and the curve denoted as "total gas energy" includes the contribution from $E_{\rm pot,gas-1}$ but not from $E_{\rm pot,gas-2}$. [Luke comments: Should be double-checked.]

The Ohlmann et al. (2016) setup allowed for a much lower pressure and lower density ambient medium. Thus, to make a direct comparison with our simulation, it was necessary to subtract from each energy term the fraction contributed by the ambient medium (or by the gravitational interaction between the ambient medium and the other components); these quantities involving the ambient gas were assumed to remain constant for the duration of the simulation. As expected from the analysis of Paper I, close agreement between results from the two simulations is apparent, in spite of the very different methodologies used. There is, however, a larger separation between the total particle energy and total gas energy curves (shown in dashed blue and dotted blue, respectively) after plunge-in in the top panel of Figure 2 as compared with the bottom panel. The particle and gas potential energies also experience larger changes during plunge-in (dashed and dotted red, respectively).

Assuming that our partitioning of the energy components mimics reasonably well that of Ohlmann et al. (2016), these differences could be caused by differences in initial conditions. Firstly, in our simulation the RG is not rotating with respect to the inertial frame of reference of the simulation, while in that of Ohlmann et al. (2016) the RG is initialized with a solid body rotation of 95% of the orbital angular speed. (The reality would lie somewhere in between and can be estimated as $\sim$ 30% of the orbital angular speed from the results of MacLeod et al. 2018). In spite of this difference, however, the inter-particle separation a reaches a smaller value ($< 10\,{\rm R}_\odot$) at the first periastron passage in the simulation of Ohlmann et al. (2016) than in that of Paper I ($14\,{\rm R}_\odot$), even though the time of this first periastron passage (i.e. the end of plunge-in) occurs at about $t = 13$ d in both simulations.

Secondly, Ohlmann et al. (2016) performed a relaxation run to set up their initial condition, while we did not, which would have led to differences in the initial stellar profiles (apart from the slight differences that would have already existed due to the slightly different MESA models employed). We note that some quantities, like internal energy (solid green) and total potential energy (solid red) remain approximately constant for the first ~ 5 d in our simulation, while showing more variation in that of Ohlmann et al. (2016). This suggests that the RG is more stable in our simulation. Part of the reason could be that we iterated over the RG core mass to obtain a smoother initial RG profile, and part of the reason could be that we used a denser and higher pressure ambient medium to stabilize the outer layers of the RG. The broad practical implication of the latter compromise is well-known: obtaining an initial condition that is both highly stable and physically realistic in CE simulations is computationally challenging. We expand on the numerical challenges involving the ambient medium in Section **??**.

In any case, we are encouraged by the close agreement between the two simulations, and take this as confirmation that our results are physical.

4 PARTIAL ENVELOPE UNBINDING

When evaluating the extent to which the envelope is unbound, it is important to be precise about the meaning of the term 'unbound.' We call the gas at a certain location in space and time unbound if its overall energy density, equal to the sum of bulk kinetic, internal and potential (due to self-gravity and interactions with both particles) energy densities is greater than or equal to zero, that is $\mathcal{E}_{\rm gas} \geqslant 0$.

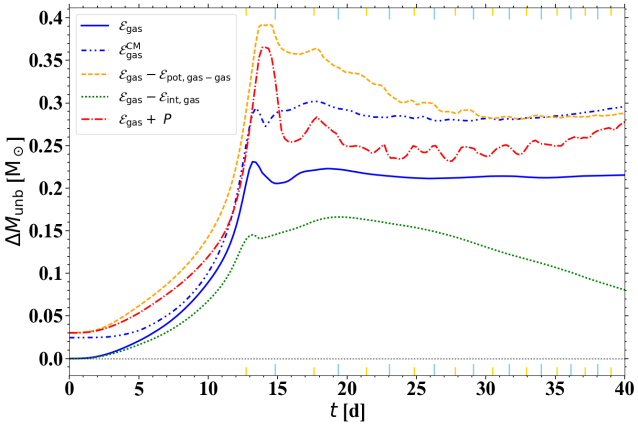

Figure 3. Change in unbound mass of the envelope with time according to the fiducial definition of 'unbound,' $\mathcal{E} \geqslant 0$ (solid blue), as well as various alternative definitions labeled in the legend (see Section 4). More precisely, $\Delta M_{\rm unb}$ represents the change in unbound mass with respect to the initial value of the unbound mass for the fiducial definition.

This definition is somewhat arbitrary and can thus be debated, but we have chosen a simple definition that is also common in the literature. For example, one could be more conservative by excluding the internal energy density, or more liberal by replacing the internal energy density by the enthalpy density, which is the sum of internal energy density and pressure (Ivanova et al. 2013, and references therein).

As we explain below in more detail, virtually all of the unbinding of material happens between the start of the simulation and end of the plunge-in phase. That this happens in spite of the negligible energy transfer between particles and gas during this time (Section 3) is counterintuitive, but can be explained by noting that the energy transfer between particles and gas is highly inhomogeneous within the envelope, as will become apparent in Section 4.2.

4.1 Unbound mass

In Figure 3 we plot the change in the unbound mass as a function of time (solid blue). Mass becomes unbound at an increasing rate from the start of the simulation until the end of plunge-in, after which the amount of unbound mass abruptly levels off. This behaviour is very similar to that obtained by Iaconi et al. (2017) in their PHANTOM simulation (see their Fig. 9, top panel for results from the run with the most comparable setup to ours; see also Iaconi et al. 2018). By $t = 40$ d the total unbound mass $\Delta M_{\rm unb} \approx 0.22\,{\rm M}_\odot$ or about 14% of the envelope mass, which happens (somewhat by chance) to be almost the same fraction obtained by Iaconi et al. (2017), who obtained 13%. Ohlmann et al. (2016) obtain a somewhat lower value of 8% by the end of their simulation. As they find that most of this is ejected during the first 40 d, the difference between their simulation and ours is again likely caused by the slightly different initial conditions.

Although the total gas energy $E_{\rm gas}$ hardly changes between $t = 0$ and the end of plunge-in at $t \approx 13$ d (Section 3), this is the time when most of the unbinding of mass happens. The reason must be that the energy density of the gas does not change by the same amount everywhere; some of the gas gains energy while the remainder loses energy, such that the net change is almost zero. To understand this in more detail, we discuss the spatial variation of the energy density in Section 4.2.

The other lines in Figure 3 represent changes in unbound mass using alternative definitions of 'unbound.' The reason that some of these curves do not start from $\Delta M_{\rm unb} = 0$ at $t = 0$ is that for presentional convenience we chose to subtract the unbound mass in the ambient medium under the standard definition of 'unbound' from each of the initial values of the unbound mass in the simulation. Thus, $\Delta M_{\rm unb}$ represents the change in unbound mass with respect to the initial value of the unbound mass for the standard definition of 'unbound,' that is $\mathcal{E}_{\rm gas} \geqslant 0$. More liberal definitions plotted are $\mathcal{E}_{\rm gas} - \mathcal{E}_{\rm pot,gas-gas} \geqslant 0$ (exclusion of self-gravity; orange dashed), $\mathcal{E}_{\rm gas} + P \geqslant 0$ (replacement of internal energy density with enthalpy density; red dashed-dotted), and $\mathcal{E}_{\rm gas}^{\rm CM_{1-2}} \geqslant 0$, where the left-hand-side is the gas energy density in the frame of the particles' centre of mass (blue dashed-double-dotted; we motivate this choice in Section 4.5). A more conservative definition is $\mathcal{E} - \mathcal{E}_{\rm int,gas} \geqslant 0$ (exclusion of the internal energy density; green dotted). If one adopts one of the more liberal prescriptions, one obtains $\Delta M_{\rm unb} \approx 0.3\,{\rm M}_\odot$, or about 19% of the total envelope mass. However, the values of $\Delta M_{\rm unb}$ corresponding to $\mathcal{E}_{\rm gas} + P \geqslant 0$ and $\mathcal{E}_{\rm gas}^{\rm CM} \geqslant 0$ are rising at the end of the simulation.

It has been argued previously that energy deposition occurs only outside the orbit of the particles (Ivanova & Nandez 2016). While the gas in between the particles is, in fact, affected by the interaction in our simulation, as is clear from the morphology seen in 2D slices of density or energy (see Section 4.2), it could perhaps still be argued that the interaction with material outside the orbit is stronger than with material inside the orbit. Then when calculating the unbound mass fraction it is interesting as an alternative to consider only the mass of the envelope that is exterior to the particle orbit, that is, to exclude the mass of gas within a sphere of radius a centred on particle 1. (We emphasize that the radius a of this sphere that demarcates the regions interior and exterior to the orbit is continuously changing with time.) When the calculation is done in this way, we find that ??% of the mass exterior to the orbit is unbound at $t = 13$ d, when the exterior mass comprises about 77% of the gas mass, and ??% of the exterior mass is unbound at $t = 40$ d, when the exterior mass accounts for about 97% of the gas mass. The material interior to the particle orbit is itself strongly bound, with ??% of the interior mass bound at $t = 13$ d and ??% bound at $t = 40$ d. The total gas energy interior to the orbit at $t = 13$ d is -1.2×10^{47} erg or about 48% of the total gas energy, while at $t = 40$ d, the gas interior to the orbit has energy -0.3×10^{47} erg or about 22% of the total gas energy. [Luke comments: Must fill in and check these numbers, needs a brief conclusion]

4.2 Spatial analysis

[Luke comments: Our analysis is not yet complete and in particular we need to understand the movie corresponding to Figure 6. To do so, we are going to plot several movies side-by-side, including gas density, Mach number, as well as each of the terms in the gas energy density (bulk kinetic, internal, potential with particle 1, potential with particle 2 and self-gravity). The same will be done for the slice orthogonal to the orbital plane and intersecting both particles, and also for the slice orthogonal to both that plane and the orbital plane and intersecting particle 2.]

In order to interpret Figure 3 and gain insight into the partial unbinding of the envelope, we explore the spatial distribution of energy and its variation with time. Figure 5 shows snapshots of the absolute value of the energy density of gas $|\mathcal{E}_{\rm gas}|$ in slices through the orbital plane at times $t = 0$, 10, 20 and 40 d. Recall that mass is defined to be 'bound' when the total energy density $\mathcal{E}_{\rm gas} < 0$ and 'unbound' when $\mathcal{E}_{\rm gas} \geqslant 0$. The dark lines on the plot (highlighting regions of very low $|\mathcal{E}_{\rm gas}|$) thus represent transitions between bound and unbound material. Contours show the gas density [Luke comments: Must update the figure and complete the discussion of the figure.]

It is helpful to define a normalized energy density $\mathcal{E}_{\rm gas,norm} = \mathcal{E}_{\rm gas}/\max(\mathcal{E}_{\rm kin,gas} + \mathcal{E}_{\rm int,gas},\ -\mathcal{E}_{\rm pot,gas})$ (where $\mathcal{E}_{\rm pot,gas} = \mathcal{E}_{\rm pot,gas-1} + \mathcal{E}_{\rm pot,gas-2} + \mathcal{E}_{\rm pot,gas-gas}$), so that $\mathcal{E}_{\rm gas,norm} = -1$ corresponds to maximally bound material while $\mathcal{E}_{\rm gas,norm} = 1$ corresponds to maximally unbound material. Slices through the orbital plane are plotted in Figure 6, with bound material coloured red and unbound material blue. Initially, much of the ambient material is unbound as a conseqence of its large internal energy density and relatively large distance from the concentration of mass near the centre of the domain. The second snapshot at $t = 10$ d shows that gas...during plunge-in....[Luke comments: complete discussion while staring carefully at sequence of figures...]

In Figure 7 we again plot $\mathcal{E}_{\rm gas,norm}$, but now for a sequence of equally spaced snapshots beginning just after plunge-in at $t = 13.0$ d and ending at about 14.4 d. Snapshots are zoomed in on the central $200\,{\rm R}_\odot$ and are shown in the reference frame centred on particle 2 (softening sphere marked in green) and corotating with the orbit of the particles, so that particle 1 is situated to the left of centre (softening sphere in black). Gas in the wake of particle 2 that is unbound/blue at $t = 13$ d apparently transitions to being bound/red by $t = 14.4$ d. This explains the decline in $\Delta M_{\rm unb}$ after $t \approx 13$ d seen in Figure 3. [Luke comments: NEEDS closer study of figures.]

4.3 Efficiency of partial envelope removal

As we saw in Section 3, orbital energy of the particles is converted to gas energy with the total energy conserved to within 5% during the simulation, and this is encapsulated by the green (particle energy), orange (gas energy) and black (total energy) lines in the top panel of Figure 1. However, not all of the particle orbital energy released goes into unbinding the envelope because some of it goes into increasing the energy of material that is already unbound ($\mathcal{E}_{\rm gas} \geqslant 0$). Since unbound material will never have exactly zero energy density, there is always an efficiency associated with the energy transfer process (see also Section 5, where we discuss the energy formalism involving the efficiency parameter $\alpha_{\rm CE}$). To get an idea about how much energy is 'wasted' in this respect, we plot various energy components with time for gas that is *unbound* in the bottom panel of Figure 1. From the orange line, we see that during the simulation about 0.2×10^{47} erg of energy is gained by the unbound gas. Granted, the mass of unbound gas increases during the first ~ 13 d, and as our code is Eulerian, individual fluid elements cannot be tracked, so it is not possible to say whether some of the unbound gas becomes bound at a later time. In spite of these caveats, it is interesting to estimate the fraction of the liberated particle orbital energy that is transferred to unbound gas. As the change in gas energy during the simulation is 1.3×10^{47} erg, the fraction that ends up in unbound gas is about 15%.

Let us now try to understand this in more detail. We see from the bottom panel of Figure 1 that most of the increase in energy of the unbound material occurs in the first 13 d. This is consistent with the change in the unbound mass $\Delta M_{\rm unb}$ also peaking at $t \approx 13$ d. The energy transferred is mainly in the form of kinetic energy, as material is launched outward during plunge-in. Subsequently, the unbound gas, whose mass remains almost constant after $t = 13$ d, transfers kinetic energy to internal energy and potential energy as it expands.

There is another way in which energy transfer to the en-

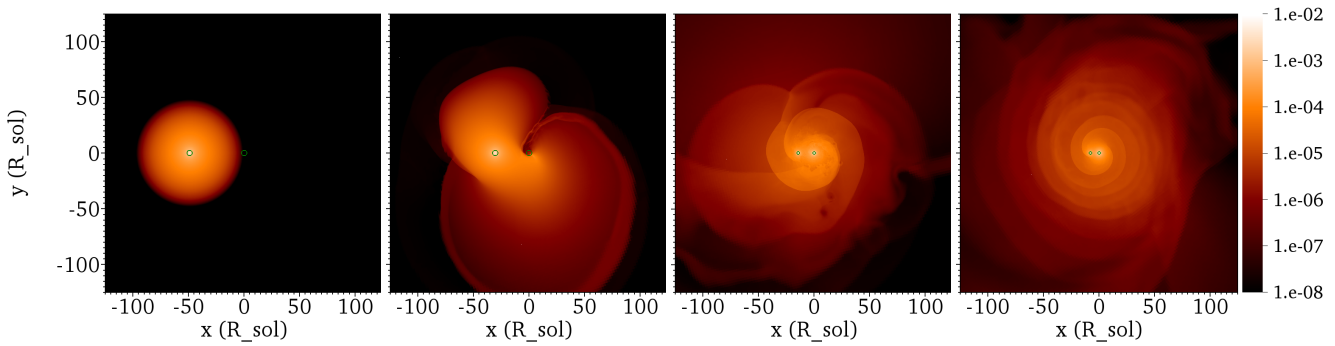

Figure 4. Density, in g cm^{-3} in a slice through the secondary and parallel to the xy (orbital) plane, for Model A (no subgrid accretion model). The secondary is positioned at the centre with the frame rotated so that the primary particle is always situated to its left (the plotted frame of reference is rotating with the instantaneous angular velocity of the particles' orbit). Both particles are denoted with a green circle with radius equal to the spline softening length. Snapshots from left to right are at t = 0, 10, 20 and 40 d. [Luke comments: Copied from Paper I.]

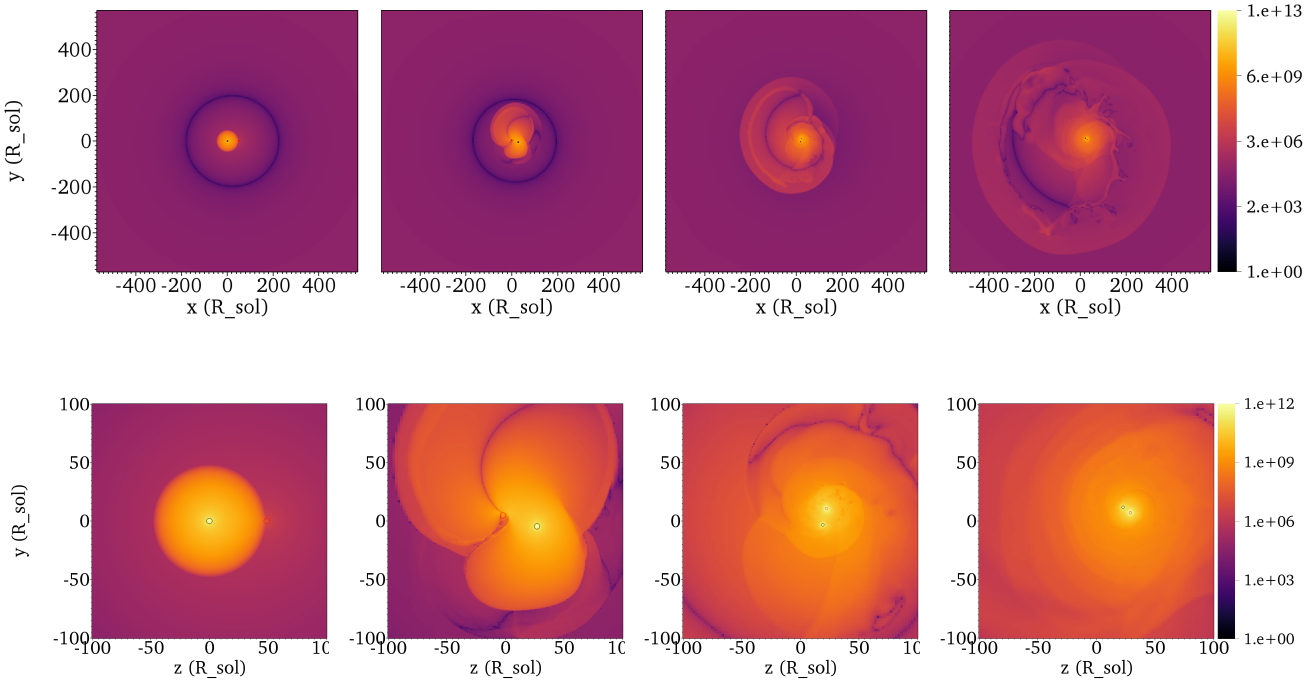

Figure 5. Snapshots showing log $|\mathcal{E}_{\rm gas}|$ at t = 0, 10, 20 and 40 d. [Luke comments: Change numbers on color bar.]

velope is inefficient. To expand, the envelope must displace ambient material, which has significant pressure and mass in our simulation. Work must be done by the envelope both against thermal pressure of the ambient material and also against gravity. These terms can respectively be estimated as $\sim (4\pi/3)P_{\rm amb}r_{\rm f}^3$ and $\sim (4\pi/3){\rm G}r_{\rm f}^2(M_1+M_2)\rho_{\rm amb}$, where $P_{\rm amb} = 1\times10^5$ dyn cm^{-2} is the ambient pressure, $\rho_{\rm amb} = 7\times10^{-9}$ g cm^{-3} is the ambient density, $M_1 = 2\,{\rm M}_\odot$ is the primary mass, $M_2 = 1\,{\rm M}_\odot$ is the secondary mass, and $r_{\rm f} \sim 3\times10^{13}$ cm is the radius of the envelope at t = 40 d. With these expressions we obtain $\sim 0.1\times10^{47}$ erg for each work term. Thus, $\sim 0.2\times10^{47}$ erg may have been transferred from the envelope to the ambient medium during the course of the simulation. This is a small amount compared to the total envelope energy, but we expect that the expansion of the envelope would have been slightly faster with a less dense or lower pressure ambient medium.[1] In any case, since we have analyzed the gas energy budget (envelope + ambient) as a whole, the energy transfer between these two components is unlikely to affect any of our conclusions. For a real star, we would expect the pressure and mass of ambient material to be less significant, though if the ambient material consists of material ejected by a stellar wind that preceded the CE interaction, then energy transfer between the envelope and ambient medium may not be negligible.

[1] Indeed we noticed a slight increase in the size of the envelope structure during plunge-in for a simulation which had initial ambient density $\rho_{\rm amb} = 1.0\times10^{-10}$ g cm^{-3} compared to a simulation that was otherwise the same but with $\rho_{\rm amb} = 6.7\times10^{-9}$ g cm^{-3}, as in the present work (respectively Models G and E described in Appendix A of Paper I). Reassuringly, the particle orbits were almost identical up to the end of the former simulation at $t \approx 10$ d.

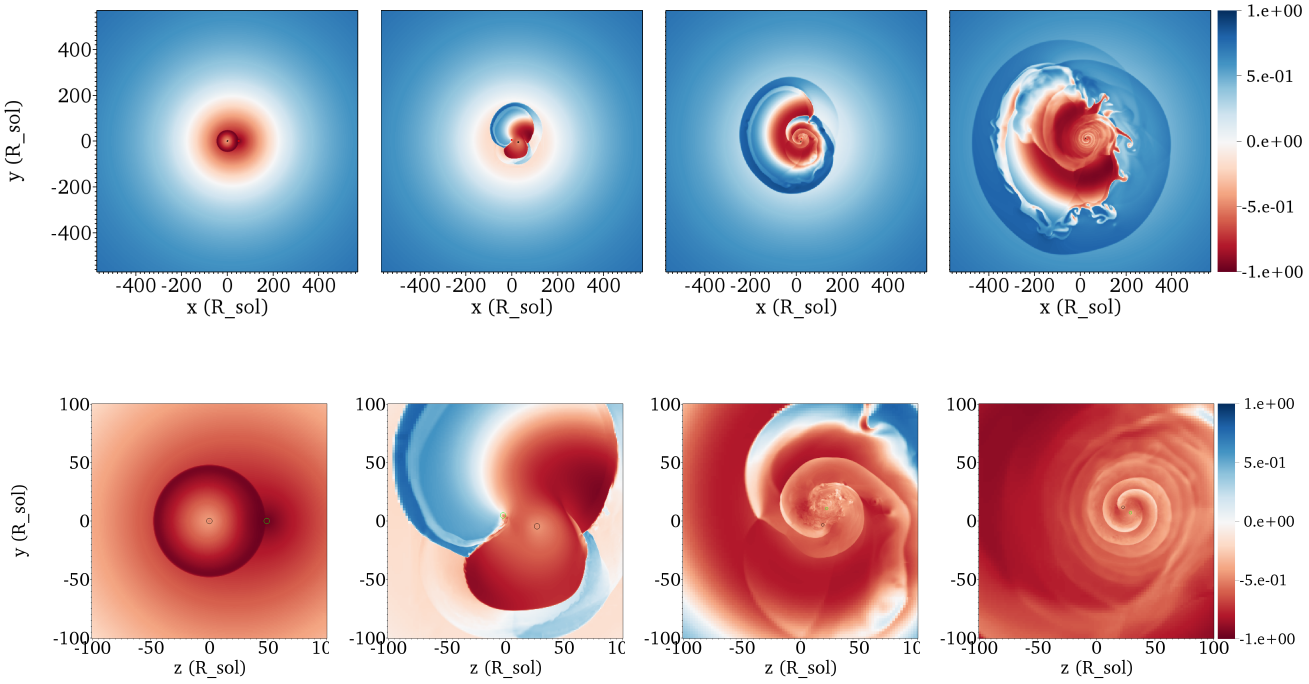

Figure 6. Snapshots of $\mathcal{E}_{\rm gas}/\max(\mathcal{E}_{\rm kin,gas}+\mathcal{E}_{\rm int,gas},-\mathcal{E}_{\rm pot,gas})$, where $\mathcal{E}_{\rm pot,gas}=\mathcal{E}_{\rm pot,gas-1}+\mathcal{E}_{\rm pot,gas-2}+\mathcal{E}_{\rm pot,gas-gas}$, in the orbital plane at $t=0$, 10, 20 and 40 d. A value of 1 corresponds to a maximally unbound system, while a value of -1 corresponds to a maximally bound system, for our standard definition of 'unbound': $\mathcal{E}_{\rm gas}\geqslant 0$. Particle 1 is shown by a black dot, while particle 2 is shown by a red dot [Luke comments: Change number format, use large circles for particle contours, different colors for these circles.]

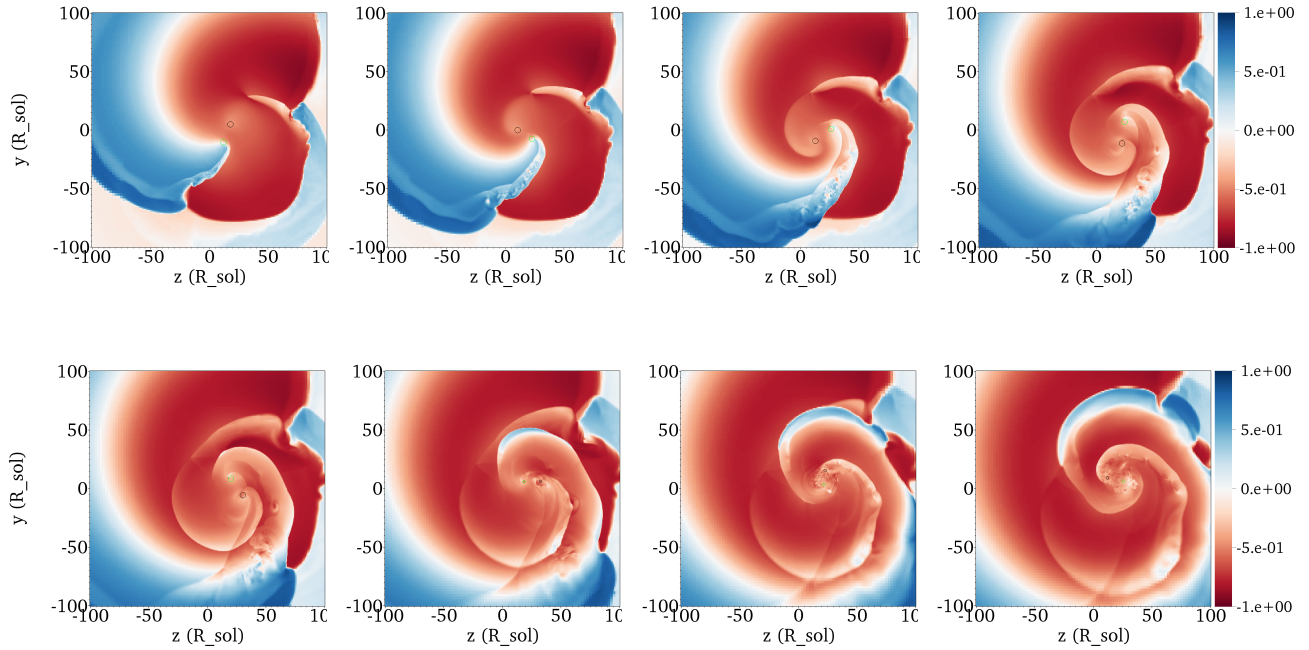

Figure 7. As Figure 6 but now showing a sequence of snapshots separated by about 0.5 d starting at $t=13.0$ d. Softening spheres are shown as black and green circles for particles 1 and 2, respectively. [Luke comments: Should thicken contour to make more visible and possibly also enlarge size to twice the softening radius. Formatting as in Figure 6.] The part of the wake of particle 2 in the central part of the envelope transitions from blue (unbound) to red (bound) during this time. [Luke comments: This plot should be in the co-orbiting reference frame so that can more easily compare snapshots by eye.]

4.4 Timescale for ejecting the envelope and fate of the remnant

From the above analysis we can make the following two general conclusions: (i) the rate of unbinding is approximately zero at the end of the simulation (for the standard definition of 'unbound'), and has generally been small since the end of plunge-in at $t \approx 13$ d; and (ii) the average rate of energy transfer from the particles to the gas is approximately constant at the end of the simulation, and equal to about 0.03×10^{47} erg d^{-1} (final average slope of orange curve of top panel of Figure 1). Of this transfer rate, about 0.001×10^{47} erg d^{-1}, a negligible fraction, is being tranferred from the particles to gas that is already unbound (final slope of orange curve of bottom panel of Figure 1). Thus, although the envelope continues to gain energy at a relatively high rate, this energy is being gained by material that is still bound by the end of the simulation.[2] Assuming this energy transfer rate of 0.03×10^{47} erg d^{-1} were to continue into the future, one can estimate how long it would take for the gas to attain zero total energy, and we find it would take an additional 38 d. However, this calculation includes the energy of the ambient medium, which initially has a net positive energy of $E_{\rm amb} \sim 0.5 \times 10^{47}$ erg. Thus, we subtract this ambient energy from the value of $E_{\rm gas}$ at $t = 40$ d given in Tab. 1 to give an envelope gas energy $E_{\rm e} \sim -1.65 \times 10^{47}$ erg, and thus the additional time needed for the envelope to attain $E_{\rm gas} = 0$ would be about 55 d.

Now, from Section 4.3 we know that not all of the liberated particle orbital energy will be transferred to bound material, and that this leads to an efficiency factor ϵ, found to be about 85% in the first 40 d (that is, 15% of the energy gets 'wasted'). Assuming an efficiency of $\epsilon = 0.85$ for the remainder of the evolution, the time calculated above must be divided by ϵ, giving ~ 65 d. With an efficiency of only 10%, the released orbital energy would have to be about 16.5×10^{47} erg, and the timescale for ejecting the envelope would be ~ 550 d, or about 1.5 yr, still very short compared to upper limits obtained from observations [Luke comments: REF?].

The orbital energy of the particles at $t = 40$ d is about $E_{1-2}(40\,{\rm d}) = -0.95 \times 10^{47}$ erg (Tab. 1). Then, since the orbit is expected to remain roughly circular, we can write

$$a_{\rm f} \sim \frac{GM_{1,{\rm c}}M_2}{2}\left(\frac{E_{\rm amb} - E_{\rm gas}(40\,{\rm d})}{\epsilon} - E_{1-2}(40\,{\rm d})\right)^{-1}. \quad (1)$$

Putting $\epsilon = 1$ gives the upper limit $a_{\rm f} \sim 2.9\,{\rm R}_\odot$, while for $\epsilon = 0.85$ we obtain $a_{\rm f} \sim 2.6\,{\rm R}_\odot$ and for $\epsilon = 0.1$ we obtain $a_{\rm f} \sim 0.4\,{\rm R}_\odot$.

Using the following estimate of the Roche-lobe radius (Eggleton 1983)

$$r_{\rm L} = \frac{0.49q^{2/3}a}{0.6q^{2/3} + \ln(1+q^{1/3})}, \quad (2)$$

where $q = M_{1,{\rm c}}/M_2 \approx 0.38$, we estimate the Roche radius of the secondary to be $r_{\rm L} \sim 0.3a$. Thus, for $\epsilon = 1$, 0.85 and 0.1, we would have $r_{\rm L} \sim 0.9\,{\rm R}_\odot$, $0.8\,{\rm R}_\odot$ and $0.1\,{\rm R}_\odot$, respectively. This would imply that mass transfer by Roche-lobe overflow would occur if the secondary was a main sequence star, but not if it was a WD.

[Luke comments: Comment on what would happen after RL overflow.]

In the simulation of Ohlmann et al. (2016), the rate of decrease of orbital energy of the particles reduces with time, and is much smaller at the end of their simulation at $t \sim 130$ d than at $t = 40$ d.

[2] This explanation assumes that bound (unbound) material after $t \approx 13$ d has for the most part remained bound (unbound). This assumption seems reasonable after studying the evolution of the 2D distribution of energy; see also Section 4.2.

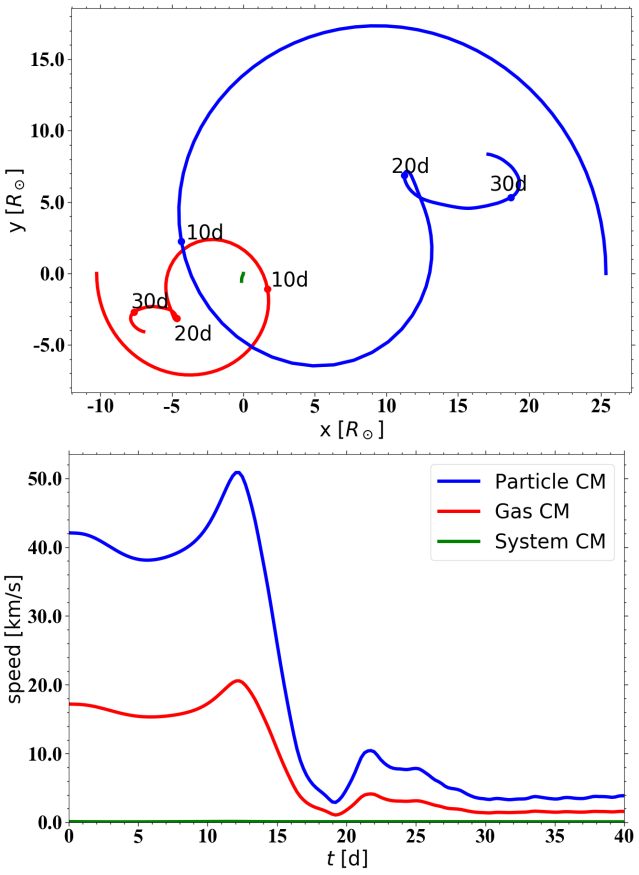

Figure 8. Top: Motion in orbital plane of the particle CM (blue), gas CM (red) and net system CM (green). The position of the system CM moves gradually in the $-y$ direction during the course of the simulation. Bottom: Evolution of the speed relative to the reference frame in which the simulation is carried out, for the particle CM (blue), gas CM (red) and net system CM (green).

This would suggest that the assumption that the rate of decrease of orbital energy remains constant is far too optimistic. On the other hand, the results of Paper I suggested that simulations of CEE may not be converged with softening length $r_{\rm soft}$ (see also Iaconi et al. 2018), as it was seen that when $r_{\rm soft}$ was decreased to ensure that the arbitrary constraint $r_{\rm soft} < a/5$ (also employed by Ohlmann et al. 2016) was satisfied, there was a marked increase in the mass flow toward the secondary, and a shift to a tighter orbit compared to the other simulation studied, for which $r_{\rm soft}$ was not reduced. Thus, the above estimates for the timescales for envelope ejection may not be overly optimistic after all. In any case, numerical studies that test convergence with softening length and resolution are, in our opinion, needed in order to make progress in this regard.

4.5 Motion of the centre of mass of the particles and relevance for PN-central star offsets

One caveat in our definition of 'unbound' is that it does not take into account the relative motion of the particle binary system and the disrupted envelope gas. The reason this might be important is that fundamentally we are interested in the extent to which gas is bound *to the particles*. In the above analysis, the kinetic energy of the particles and bulk kinetic energy of the gas are given in the inertial reference frame of the simulation, which, assuming perfect

conservation of linear momentum (see below) is the centre of mass (CM) reference frame of the system. In general, however, the CM of the particles and that of the gas are in relative motion, moving in opposite directions in the simulation frame such that overall linear momentum is approximately conserved. Given the significant asymmetry of the gas distribution in the orbital plane, and its rapid evolution with time, we might expect significant relative motion of the particle and gas centres of mass, and this is indeed the case. Moving to the reference frame of the particle CM, and neglecting non-inertial effects, one sees that the bulk kinetic energy of gas would be evaluated as $E_{\rm kin,gas}^{\rm CM_{1-2}} = \frac{1}{2}\int \rho(\boldsymbol{x})|\boldsymbol{v}(\boldsymbol{x}) - \boldsymbol{v}_{\rm CM,1-2}|^2 {\rm d}\boldsymbol{x}$. This alternative definition would mean that gas whose speed relative to the particle CM is larger (smaller) than its speed relative to the system CM is more (less) unbound. On the whole, since the envelope CM and particle CM are moving in opposite directions, one expects this to lead to an increase in the total mass of unbound gas, as confirmed by comparing the dashed-double-dotted blue and solid blue lines in Figure 3.

We present data for the motion of the particle CM and gas CM in Figure 8, which shows the path traced in the orbital plane by the particle CM (blue), gas CM (red), and system CM (green) in the top panel, and their respective speeds as a function of time in the bottom panel. As expected, the position of the system CM is approximately constant, and its speed is at all times is very small ($< 0.2\,{\rm km\,s^{-1}}$); deviations in the position imply the presence of small errors in linear momentum conservation. [Luke comments: Must redo this plot for full resolution data. The discrepancy cannot be accounted for by inflow from the boundary for the de-resolved analysis. We know that non-conservation of mass is accounted for by inflow.] We now turn to the bottom panel, where the speed of the particle CM is plotted against time in blue, that of the gas CM in red, and that of the system CM in green. We see that until the end of the plunge-in phase at $t \approx 13\,{\rm d}$, the relative speed between the gas CM and particle CM (obtained by adding the red and blue curves) is 53-71 $\rm km\,s^{-1}$, and the final relative speed is about 5 to 6 $\rm km\,s^{-1}$. This relative motion leads to a small but non-negligible increase in the gas bulk kinetic energy, and hence the mass of unbound material (if this alternative definition of 'unbound' is adopted). Although this effect is relatively unimportant in the present context, it could be more important in other contexts, and should be accounted for.

Another, different effect of this relative motion between gas CM and particle CM is even more interesting. In several bipolar PNe, it has been observed that the binary central star is offset from the centre of the PN, and it is believed that these offsets are caused by the binarity (e.g. MyCn 18: Sahai et al. 1999; Clyne et al. 2014; Miszalski et al. 2018; Hen 2-161: Jones et al. 2015; Abell 41: Jones et al. 2010). The best studied example is the Etched Hourglass Nebula MyCn 18, and various possible explanations have been explored to explain the offset of the PN central star from the geometric centre of the nebula, but all of these are found to fail (Miszalski et al. 2018, and references therein).

The observed distance to MyCn 18 is 618 ± 101 au (Miszalski et al. 2018) and the estimated time since the end of the CE phase is ~ 2700 yr (Clyne et al. 2014; Miszalski et al. 2018). This implies a mean velocity of ~ 1 $\rm km\,s^{-1}$ of the PN central star with respect to the nebula in the plane of the sky, if the motion started at the end of the CE phase. Thus, the velocities we obtain for the particle CM at the end of our simulation of ~ 4-6 $\rm km\,s^{-1}$ (relative to the inertial frame and to the envelope CM, respectively) are of the same order of magnitude. The direction of the offset is within 5° of the PN minor axis, which presumably is parallel to the orbital plane of the binary. This agrees with the motion of the particle CM in our simulation, whose velocity in the z-direction perpendicular to the orbital plane has magnitude $\leqslant 0.3\,{\rm km\,s^{-1}}$ during the simulation, with average z-velocity only $-6\times10^{-3}\,{\rm km\,s^{-1}}$ between $t = 30\,{\rm d}$ and $t = 40\,{\rm d}$. We might expect the velocities in the MyCn 18 system to be smaller than in our simulation since the binary components are less massive (Miszalski et al. 2018 obtain primary and secondary masses of $0.6\pm0.1\,{\rm M_\odot}$ and $0.19\pm0.05\,{\rm M_\odot}$ respectively, whereas in our cases the particle masses are $M_{1,\rm c} = 0.4\,{\rm M_\odot}$ and $M_2 = 1\,{\rm M_\odot}$). On the other hand, we are seeing only a plane of the sky projection, so the full 3D offset may be somewhat larger, which would imply a correspondingly larger velocity for the central star in MyCn 18. In any case, the relative motion between the particle CM and envelope seen in our simulation, caused by the asymmetry in the morphology of the disrupted CE in the orbital plane, leads to velocities in the orbital plane comparable to those needed to explain the offsets of PN central stars. We therefore propose this as a possible mechanism for such offsets, but more work is need, for example, efforts to simulate specific systems such as MyCn 18.

5 ENERGY FORMALISM AND $\alpha_{\rm CE}$ PRESCRIPTION

A popular approach for studying the CE phase is by means of the so-called energy formalism. Here we focus on the prescription from the review Ivanova et al. (2013) [equivalent to their equation (3)]:

$$\frac{GM_1M_{1,\rm e}}{\lambda R_1} = \alpha_{\rm CE}\frac{GM_{1,\rm c}M_2}{2}\left(\frac{1}{a_{\rm f}} - \frac{M_1/M_{1,\rm c}}{a_{\rm i}}\right), \tag{3}$$

where $M_{1,\rm e} = M_1 - M_{1,\rm c}$, the quantities $\alpha_{\rm CE}$ and λ are parameters, subscripts i and f stand for initial and final, respectively, and for the formula to be valid 'final' refers to the time at which the envelope becomes completely unbound (eliminating the drag, and thus halting the inspiral). On the left-hand-side (LHS) we have the envelope 'binding energy,' which includes the negative of the potential energy due to the gas-particle 1 gravitational interaction as well as that due to gas self-gravity. This involves the parameter λ, which can be calculated from first principles provided the envelope density profile is known.[3] The definition of 'binding energy' in this context may also include the negative of the envelope internal energy, in which case the equation of state must also be known to compute λ (below we assume that the internal energy is included in the binding energy). The right-hand-side (RHS) is the energy that is used to unbind envelope gas, and is equal to the negative of the change in the orbital energy of the system between $t = t_{\rm i}$ when $a = a_{\rm i}$ and $t = t_{\rm f}$, when $a = a_{\rm f}$, multiplied by the efficiency $\alpha_{\rm CE}$. Even if we assume that all sources and sinks of energy have been accounted for, we expect $\alpha_{\rm CE} < 1$ because unbound material will in general have $\mathcal{E}_{\rm gas} > 0$, not $\mathcal{E}_{\rm gas} = 0$ (see also Section 4.3).

We hereby propose the following alternative prescription:

$$GM_{1,\rm e}\left[\frac{M_1}{\lambda R_1} + \frac{M_2}{2a_{\rm i}}\left(2 - \frac{M_2}{M_1+M_2}\right)\right] = \alpha_{\rm CE}\frac{GM_{1,\rm c}M_2}{2}\left[\frac{1}{a_{\rm f}} - \frac{1}{a_{\rm i}}\left(2 - \frac{M_1^2/M_{1,\rm c} + M_2}{M_1+M_2}\right)\right]. \tag{4}$$

With the intention of making the equation more intuitive and logical from an accounting standpoint, we have kept all terms contributing to $E_{\rm gas}$ on the LHS, and all terms contributing to E_{1-2} on the RHS.[4]

[3] Alternatively, λ can be combined with $\alpha_{\rm CE}$, resulting in a single parameter $\lambda\alpha_{\rm CE}$.

[4] In this section we do not differentiate between 'gas' and 'envelope'; that is we neglect contributions from the ambient medium. When we apply the

Equation (4) makes use of the relations $v_1^2 = G\mu m_2/(am_1)$ and $v_2^2 = G\mu m_1/(am_2)$ for the particle speeds in the inertial CM frame in the standard two-body problem, assuming a circular orbit and with $\mu = m_1 m_2/(m_1 + m_2)$ the reduced mass. The difference from equation (3) is that the initial orbital energy involving the envelope and particle 2 is now on the LHS, and does not get multiplied by $\alpha_{\rm CE}$. As a result, equations (3) and (4) are equivalent if and only if $\alpha_{\rm CE} = 1$. Thus, equation (4) tells us how particle energy has been converted with an efficiency $\alpha_{\rm CE}$ into gas energy during the envelope unbinding process. The orbital energy $E_{\rm kin,gas,i} + E_{\rm pot,gas-2,i} < 0$ contributes to the negative binding energy of the envelope, and thus multiplying it by $\alpha_{\rm CE}$, as done in equation (3), is not, in our view, well motivated. Doing so implies an effective reduction in the overall binding energy, so that using equation (3) underestimates the energy required to unbind the envelope. As we discuss in the next section, equations (3) and (4) tend to lead to similar results in practice.

5.1 Applying the energy formalism

Now that we have summarized the energy formalism, we can use it to assess whether the simulation results are consistent with theoretical expectations. To apply the formalism, we have evaluated the various energy terms of Tab. 1 at $t = 0$, but now for the envelope alone excluding the ambient medium. The values are listed in the fourth column of Tab. 2. Where there is a small difference between a value from Tab. 2 and the corresponding value in the fourth column of Tab. 1, we have verified that it is accounted for by the energy in the ambient medium.

To proceed, we first evaluate the left-hand and right-hand sides of equations (3) and (4), for $a_{\rm i} = 49\,{\rm R}_\odot$ and $a_{\rm f} = 7\,{\rm R}_\odot$, which is the approximate mean inter-particle separation at $t = 40\,{\rm d}$. For the RG in our model, λ evaluates to 1.31. Technically speaking, equations (3) and (4) are only relevant if $a_{\rm f}$ corresponds to the inter-particle separation after the envelope is completely unbound. Since this is *not* the case at $t = t_{\rm f}$ in the simulation, we cannot use the simulation along with equation (3) or (4) to obtain $\alpha_{\rm CE}$. However, we can check whether we should *expect* the envelope to be unbound at $a = 7\,{\rm R}_\odot$, given a reasonable estimate for $\alpha_{\rm CE}$.

The LHS and RHS of equations (3) and (4) for the simulation are given in Tab. 3, in the first and third rows, respectively. We see that for the LHS and RHS to be equal, a value of $\alpha_{\rm CE}$ larger than 1, and somewhere in the range 2–5, would be required. Since $\alpha_{\rm CE} > 1$ would be unphysical, this implies that we should *not expect* the envelope to be unbound at $a = 7\,{\rm R}_\odot$, which is consistent with the simulation results. Thus, that complete envelope unbinding has not been attained by the end of the simulation should not be taken as evidence that the simulation is somehow deficient. On the contrary, the simulation and the theory are in agreement.

In a real system, it may be preferable to associate the initial state at $t = t_{\rm i}$ with the Roche lobe overflow stage, which occurs just prior to CEE (MacLeod et al. 2018). This would imply a larger value of $a_{\rm i}$, which would lead to smaller contributions from the terms ($\propto 1/a_{\rm i}$) that differ between equations (3) and (4). For the system studied in this work, the Roche limit can be estimated from equation (2) to be $a_{\rm i} \approx 109 R_\odot$, which would lead to a reduction in $a_{\rm i}$-dependent terms by more than a factor of two. Values of the initial energy terms for $a_{\rm i} = 109\,{\rm R}_\odot$ are given in the fifth column of Tab. 2. In the second and fourth rows of Tab. 3, we present the LHS and RHS for this larger initial separation, for equations (3) and (4), respectively. Increasing the initial separation results in more orbital energy that can be tapped by the envelope, making it easier to unbind, and hence leading to a smaller required $\alpha_{\rm CE}$. However, the difference from the case where $a_{\rm i} = 49\,{\rm R}_\odot$ can be seen to be rather small, and anyway $\alpha_{\rm CE} > 1$ would still be required. Therefore, failure to unbind the envelope at $a = a_{\rm f} \approx 7\,{\rm R}_\odot$ does not stem from neglecting the extra orbital energy that would be gained by starting with $a = a_{\rm i} = 109\,{\rm R}_\odot$ instead of $49\,{\rm R}_\odot$. We can conclude that to achieve unbinding, one would presumably have to wait until a decreases to a considerably smaller value. Let us now estimate this final separation.

5.2 Predicting the final inter-particle separation

It is possible to predict the value of $a_{\rm f}$ for our system for a given value of $\alpha_{\rm CE}$. To do this, we can use either equation (3) or equation (4), with either $a_{\rm i} = 49\,{\rm R}_\odot$ (simulation) or $a_{\rm i} = 109\,{\rm R}_\odot$ (Roche limit). The values are given in the top half of Tab. 4 for a set of plausible choices for $\alpha_{\rm CE}$ between 0.1 and 0.5, as well as for $\alpha_{\rm CE} = 1$, for comparison. Tab. 4 tells us that we do not expect envelope ejection to occur until a has reduced to less than $3\,{\rm R}_\odot$, and likely less than $1\,{\rm R}_\odot$. This is much smaller than the final separation in our simulation, but also smaller than that of Ohlmann et al. (2016), who used very similar initial conditions and evolved the system to $t \sim 130\,{\rm d}$, at which time $a \approx 4\,{\rm R}_\odot$. Thus, it is not surprising that the envelope did not eject in the simulation of Ohlmann et al. (2016) either.

The implication is that to get the envelope to eject, one should wait longer for the separation to reduce further. This possibility was considered in Sec. 4.4, where it was pointed out that even at the end of the simulation at $t = 40\,{\rm d}$, energy was being tranferred from particles to gas at an almost steady average rate (see also Fig. 1), and that if this were to continue to late times, the envelope might be ejected by $\sim 10^2$–$10^3\,{\rm d}$, still small enough to account for observations of PPNe, which have ages $> 10^3\,{\rm yr}$ [Luke comments: must check]. The scenario envisioned by Clayton et al. (2017) wherein fallback of envelope material occurs, leading to multiple successive CE phases, could also play a role in unbinding the envelope over long timescales [Luke comments: must check that paper for details]. Nevertheless, the orbital separation does *appear*, from Fig. 1 of Ohlmann et al. (2016), to be approaching an asymptotic value, while the energy transfer rate reduces with time (their Fig. 2). This suggests that running the simulation for longer might not actually lead to envelope unbinding, but they estimate that it would take $\sim 100\,{\rm yr}$ to eject the envelope if unbinding was to continue at the final rate. Although such long timescales cannot a priori be ruled out, there is no guarantee that the envelope would eject on even these timescales. [Luke comments: Can it be argued from observations of CE (luminous red novae) that the timescale must be short in at least some cases? Must look into this.] Thus, it is worth considering alternative explanations.

6 LIMITATIONS OF SIMULATIONS AND IMPLICATIONS FOR ENVELOPE UNBINDING

Simulations have not yet resulted in the envelope becoming unbound without invoking an additional energy source, namely recombination energy (Nandez et al. 2015; Nandez & Ivanova 2016; Ivanova & Nandez 2016). Without recombination energy, the envelope is typically unbound at a level of only $\sim 10\%$ of its mass by the end of the simulation. Incorporation of the recombination energy was implemented using a simple subgrid prescription that assumes that

energy formalism to interpret the simulation in the next section, we exclude the ambient medium.

the latent energy released by recombination is absorbed locally, and does not account for transport of energy by radiation or convection. The extent to which this assumption is justified is currently being vigorously debated (Sabach et al. 2017; Grichener et al. 2018; Ivanova 2018). Another candidate for an additional energy source is the fraction of the gas energy that is released to the envelope as gas accretes onto the secondary (Soker 2004; Nordhaus & Blackman 2006; Ricker & Taam 2008, 2012; MacLeod et al. 2017; Murguia-Berthier et al. 2017; Soker 2017; Shiber & Soker 2018; Chamandy et al. 2018) [Luke comments: please insert other references if required] but it is not yet clear whether such accretion would be quenched by feedback.

Although sources (or sinks) of energy not included in our simulation may play a role, we feel that an effective approach is to first evaluate more mundane explanations before appealing to new physical ingredients, when these ingredients have not, in our view, conclusively been shown to be important. With this in mind, we sketch the following narrative, involving numerical limitations, and the non-optimal region of parameter space simulators are "pushed into" by such limitations, as a possible explanation for why complete envelope unbinding has so far not been reported in simulations without extra energy sources.

6.1 Numerical limitations

As global CE simulations are numerically highly demanding, modelers have so far focused on a similar region of parameter space, involving low-mass RGB primaries. However, as we have argued in Sec. 5.2, supported by the results presented in Tab. 4, the final separation needed to eject the envelopes in such systems is likely to be $\lesssim 1\,\mathrm{R}_\odot$. The softening length tends to be $\gtrsim 1\,\mathrm{R}_\odot$, and when the softening length was halved at $t = 16.7\,\mathrm{d}$ in our simulation, from $2.4\,\mathrm{R}_\odot$ to $1.2\,\mathrm{R}_\odot$, there was a significant effect on the orbit and mass inflow toward the secondary, even though a exceeded five softening lengths at that time (the same universal criterion used by Ohlmann et al. 2016). This suggests that our simulation is not fully converged with respect to the softening length. A similar conclusion was also reached by Iaconi et al. (2018) with respect to their simulations. It also suggests that decreasing the softening length during the simulation may lead to significant differences, e.g. in the orbit, compared to a more accurate but hypothetical simulation for which the softening length was kept constant at its smallest value from $t = 0$.[5]

Convergence studies are needed to establish the importance of numerical effects. It is possible that a too-large softening length or inadequate resolution near the particles can lead to an artificial stagnation of $\dot{a}$ for small a, and that for real systems a would decay more rapidly than in the simulations, eventually leading to either envelope expulsion or a merger. The idea that numerical limitations could be stalling the orbital decay is supported to some extent by the comparison of final separations for simulations and observations compiled from the literature and presented in Fig. 15 of Iaconi et al. (2017). However, that explanation is unlikely to be the whole story.

[5] The latter is difficult to achieve in practice since the volume resolved at the highest refinement level tends to be higher at the beginning of the simulation and the softening length must be resolved by some minimum number of cells to avoid other numerical problems, like less accurate energy conservation.

6.2 Parameter space limitations

As mentioned above, simulations tend to focus on systems involving RGB primaries, which are more compact than their AGB counterparts, and hence have a larger binding energy. It follows that the final separation needed for envelope ejection for CEE involving an AGB primary should be significantly larger than for CEE involving an RGB primary. To explore this possibility, the energy terms for an AG from the same ZAMS $2\,\mathrm{M}_\odot$ MESA (Paxton et al. 2011, 2013, 2015) simulation were evaluated and are presented in the sixth and seventh columns of Tab. 2 for an initial separation just outside the AG surface or at the Roche limit separation, respectively. That is, $a_\mathrm{i} = 124\,\mathrm{R}_\odot$ (compared to the AG radius of $122\,\mathrm{R}_\odot$) or $284\,\mathrm{R}_\odot$, computed from equation (2). The AG density and pressure profiles were calculated using the same procedure as for the RG, and with the same core cutoff radius of $2.4\,\mathrm{R}_\odot$ (chosen to be equal to the softening length; see Ohlmann et al. 2017; Chamandy et al. 2018 for details). This results in an AG of mass $1.8\,\mathrm{M}_\odot$ with a $0.5\,\mathrm{M}_\odot$ core (compared to $2.0\,\mathrm{M}_\odot$ and $0.4\,\mathrm{M}_\odot$ for the total mass and core mass of the RG). The total initial energy of the envelope is indeed much smaller in magnitude for the AG than for the RG (this is also helped by the larger initial separation a_i).

Next we turn to the predicted values of a_f for given values of α_CE in Tab. 4. We see that a_f is predicted to be almost four times larger for CEE involving the AGB star than for the RGB star. Assuming $\alpha_\mathrm{CE} \sim 0.2$–$0.3$ [Luke comments: need estimate from literature perhaps], this would suggest that most of the close low mass binary systems observed to have orbital separations $> 1\,\mathrm{R}_\odot$ are evolved from systems involving AGB, rather than RGB, stars. A caveat is that we have not considered how this result would depend on the parameter values, which can vary considerably depending on the giant and secondary masses. [Luke comments: Insert small α asymptotic limit and discuss dependence on various parameters.]

Another caveat is that to make a statement about the likelihood of a given system being the progenitor of an observed system, one must possess knowledge about the prior relative likelihood of progenitor systems. Let us assume the distribution of binary stellar separations for systems that will result in a CE phase to be approximately flat....[Luke comments: need to find this from literature]. If the ratio of AG to RG radius is 2.5, as it is for the example of a ZAMS $2\,\mathrm{M}_\odot$ star used in this work, then we would expect the ratio of CE systems involving an AGB star to those involving an RGB star of the same ZAMS mass to be of the order $(2.5-1)/1$, or $3:2$. [Luke comments: Comment on stars of a different ZAMS mass, using literature estimates of the radii] Thus, our tentative conclusion that most systems with $a > 1\,\mathrm{R}_\odot$ have evolved from primary systems involving AGB stars gains support.

6.3 The challenges of simulating CEE involving AGB stars

7 SUMMARY AND CONCLUSIONS

References

Carroll-Nellenback J. J., Shroyer B., Frank A., Ding C., 2013, Journal of Computational Physics, 236, 461

Chamandy L., et al., 2018, preprint, (arXiv:1805.03607)

Clayton M., Podsiadlowski P., Ivanova N., Justham S., 2017, MNRAS, 470, 1788

Clyne N., Redman M. P., Lloyd M., Matsuura M., Singh N., Meaburn J., 2014, A&A, 569, A50

Cunningham A. J., Frank A., Varnière P., Mitran S., Jones T. W., 2009, ApJS, 182, 519
Eggleton P. P., 1983, ApJ, 268, 368
Grichener A., Sabach E., Soker N., 2018, preprint, (arXiv:1803.05864)
Iaconi R., Reichardt T., Staff J., De Marco O., Passy J.-C., Price D., Wurster J., Herwig F., 2017, MNRAS, 464, 4028
Iaconi R., De Marco O., Passy J.-C., Staff J., 2018, MNRAS, 477, 2349
Ivanova N., 2018, ApJ, 858, L24
Ivanova N., Nandez J. L. A., 2016, MNRAS, 462, 362
Ivanova N., et al., 2013, ARA&A, 21, 59
Jones D., et al., 2010, MNRAS, 408, 2312
Jones D., Boffin H. M. J., Rodríguez-Gil P., Wesson R., Corradi R. L. M., Miszalski B., Mohamed S., 2015, A&A, 580, A19
Kruckow M. U., Tauris T. M., Langer N., Szécsi D., Marchant P., Podsiadlowski P., 2016, A&A, 596, A58
Kuruwita R. L., Staff J., De Marco O., 2016, MNRAS, 461, 486
MacLeod M., Antoni A., Murguia-Berthier A., Macias P., Ramirez-Ruiz E., 2017, ApJ, 838, 56
MacLeod M., Ostriker E. C., Stone J. M., 2018, preprint, (arXiv:1803.03261)
Miszalski B., Manick R., Mikołajewska J., Van Winckel H., Iłkiewicz K., 2018, PASA, 35, e027
Murguia-Berthier A., MacLeod M., Ramirez-Ruiz E., Antoni A., Macias P., 2017, ApJ, 845, 173
Nandez J. L. A., Ivanova N., 2016, MNRAS, 460, 3992
Nandez J. L. A., Ivanova N., Lombardi Jr. J. C., 2014, ApJ, 786, 39
Nandez J. L. A., Ivanova N., Lombardi J. C., 2015, MNRAS, 450, L39
Nordhaus J., Blackman E. G., 2006, MNRAS, 370, 2004
Ohlmann S. T., Röpke F. K., Pakmor R., Springel V., 2016, ApJ, 816, L9
Ohlmann S. T., Röpke F. K., Pakmor R., Springel V., 2017, A&A, 599, A5
Passy J.-C., Mac Low M.-M., De Marco O., 2012, ApJ, 759, L30
Paxton B., Bildsten L., Dotter A., Herwig F., Lesaffre P., Timmes F., 2011, ApJS, 192, 3
Paxton B., et al., 2013, ApJS, 208, 4
Paxton B., et al., 2015, ApJS, 220, 15
Ricker P. M., Taam R. E., 2008, ApJ, 672, L41
Ricker P. M., Taam R. E., 2012, ApJ, 746, 74
Sabach E., Hillel S., Schreier R., Soker N., 2017, MNRAS, 472, 4361
Sahai R., et al., 1999, AJ, 118, 468
Sandquist E. L., Taam R. E., Chen X., Bodenheimer P., Burkert A., 1998, ApJ, 500, 909
Sandquist E. L., Taam R. E., Burkert A., 2000, ApJ, 533, 984
Shiber S., Soker N., 2018, MNRAS,
Soker N., 2004, New Astron., 9, 399
Soker N., 2017, MNRAS, 471, 4839
Staff J. E., De Marco O., Macdonald D., Galaviz P., Passy J.-C., Iaconi R., Low M.-M. M., 2016a, MNRAS, 455, 3511
Staff J. E., De Marco O., Wood P., Galaviz P., Passy J.-C., 2016b, MNRAS, 458, 832